Hybrid Suspension/Solution Precursor Plasma Spraying of a Complex $Ba(Mg_{1/3}Ta_{2/3})O_3$ Perovskite: Effects of Processing Parameters and Precursor Chemistry on Phase Formation and Decomposition

Huidong Hou[a,b], Jocelyn Veilleux[a§], François Gitzhofer[a], Quansheng Wang[b], Ying liu[b]

[a]University of Sherbrooke, Sherbrooke, Quebec, J1K 2R1, Canada

[§] jocelyn.veilleux@usherbrooke.ca

[b]Beijing Institute of Technology, Beijing, 100081, China

Abstract $Ba(Mg_{1/3}Ta_{2/3})O_3$ (BMT) has a high melting point and is envisioned as a thermal barrier coating material. In this study, a hybrid suspension/solution precursor plasma spray process with a radio frequency thermal plasma torch is designed to deposit BMT nanostructured coatings. Six combinations of chemical reagents are investigated as coating precursors: one BMT powder suspension and five Ta_2O_5 suspensions in nitrate- or acetate-based solutions. X-ray photoelectron spectroscopy (XPS) is used to evaluate the element evaporation during plasma spraying, while a thermogravimetric / differential thermal analysis (TG/DTA) is applied to investigate the BMT formation. Parameters such as precursor chemistry, plasma power, spraying distance and substrate preheating are studied with regards to the coating phase structure. Twice the Mg stoichiometric amount with a power of 50 kW shows the best results when using nanocrystallized Ta_2O_5 as a tantalum precursor. When choosing nitrates as Ba and Mg precursors, crystallized BMT is obtained at lower plasma power (45 kW) when

compared to acetates (50 kW). $BaTa_2O_6$, $Ba_3Ta_5O_{15}$, $Ba_4Ta_2O_9$, $Mg_4Ta_2O_9$ are the main secondary phases observed during the BMT coatings deposition. Because of the complicated acetate decomposition process, the coating deposition rate from nitrate precursors is 1.56 times higher than that from acetate precursors.

Keywords BMT, hybrid SPS/SPPS, spraying parameters, precursor chemistry, decomposition

1. Introduction

High-temperature components used in modern turbines need to endure high temperature service environments (Ref 1). In order to increase turbine thermal efficiency and decrease energy consumption, these temperatures were continuously increased up to a point where they led to early failure and spallation of the most widely used thermal barrier coatings (TBCs), based on yttria-stabilized zirconia (YSZ) (Ref 2). This triggered a widespread exploration of new TBCs materials. $Ba(Mg_{1/3}Ta_{2/3})O_3$ (BMT) which was considered as the most refractory oxide ever known to science (with a melting temperature around 2900-3100 °C) (Ref 3), has been chosen as a TBCs candidate material in this study. First studied as a dielectric material, BMT showed poor sintering ability even at temperatures as high as 1600 °C (Ref 4). This demerit as a dielectric material becomes the merit of BMT as a TBC. Compared to YSZ (melting point of 2700 °C), which sinters significantly from 1200 °C (Ref 2), BMT is proposed for service at higher temperatures since its melting point and sintering temperatures are higher. Such a high melting temperature requires a plasma process which can heat BMT into well-melted or semi-molten state and then deposit BMT coatings effectively. As such, the conventional BMT coating deposition method is Air Plasma Spraying (APS) of a BMT powder. The as-sprayed BMT coatings produced by APS typically show a mixture of secondary phase (Mg-depleted phase) and BMT, which leads to a decrease in melting temperature and low mechanical properties (Ref 5-7). This problem is mainly caused by the Mg-evaporation during APS. An excess of Mg added to the initial precursors and suitable deposition parameters should remedy this problem. In addition,

commercial BMT powders are not broadly available and feedstock powder of APS requires several preparation steps including synthesis, agglomeration and sintering steps. Therefore, it is preferable to start with precursors instead of BMT feedstock from an economical standpoint. In suspension plasma spraying (SPS) (Ref 8), submicrometer or nanometer sized powders dispersed in various solvents (usually water or ethanol) are used as feedstock, while dissolved chemical reagents (salts or metal alkoxides) are fed in solution precursor plasma spraying (SPPS) (Ref 9). In SPPS, the complex feedstock preparation process of APS described above (synthesis, agglomeration and sintering of powders) is eliminated, as it occurs in-flight. As-sprayed coatings prepared by SPS or SPPS show characteristic microstructures such as submicron or nanosized pores, segmented cracks and columns (Ref 10-13), and most of them are proven or foreseen beneficial for the performance of TBCs in comparison to APS-deposited coatings. Still, as most direct current (D.C.) plasma torches use radial feedstock injection, the deposited coatings in SPS and SPPS often contain a large amount of unmolten nanosized particles that result from the overspray (Ref 13). With axial injection, overspray is less likely as the feedstock is directly fed in the core of the plasma jet. This strategy is chosen in this study to feed a radio frequency inductively-coupled plasma (R.F. ICP) torch, which is also attractive to spray refractive materials such as BMT, owing to long residence times (Ref 14, 15). The BMT precursors consist of Ta_2O_5 powders, cheaper and easier to process than Ta alkoxides, in suspension in a solution of Ba and Mg soluble salts, calling for a novel hybrid SPS/SPPS process (Ref 16). Feedstock and deposition parameters such as precursor chemistry, Mg content,

substrate pre-heating, spraying distance and plasma power are investigated with regards to the phase composition of the deposited coatings. The conditions leading to a relatively pure BMT phase are identified and discussed.

2. Experimental procedures

2.1 Feedstock preparation

Six combinations of suspensions/solutions were used in this work, as seen in Table 1. A mixture of water and ethanol was chosen as solvent. Water is required to dissolve Ba salts, but its evaporation consumes much more energy than ethanol once injected in the plasma. Ethanol also releases heat and increases temperature upon its combustion along the plasma jet (Ref 15). A constant solid concentration of 10 wt. % was chosen for all the suspension/solutions. Precursor S1 was used to investigate the phase decomposition during plasma spraying. Precursors S2, S3 and S4, with different Mg stoichiometric ratios, aimed at evaluating the influence of Mg depletion in the plasma. Regarding the solute chemistry, acetate-based precursors have a higher solubility in water compared to nitrate-based ones. As such, with acetate-based solutes, one can increase the ethanol:water ratio while keeping the same salt concentration. Thus, S4 and S5, with different salts and solvent ratios, were used to compare the effect of precursor chemistry. Precursor S5, which contains a higher percentage of ethanol, was selected to study the heating effect. Finally, precursor S6 aimed at evaluating the effect of initial Ta_2O_5 particle size. The detailed preparation of each precursor follows.

2.1.1 BMT powder for SPS

A stoichiometric BMT powder was synthesized from the mixture of Ta_2O_5, $BaCO_3$ and MgO in a muffle furnace (HEFEI KE JING Materials Technology Co., LTD., China) at 1400 °C for 2h. This synthesized BMT powder is to be used as benchmark for phase composition and to prepare a conventional suspension for SPS (precursor S1). This synthesized BMT powder was also post-calcined for 2h at different temperatures (1100 °C - 1600 °C) to analyze the ordering degree and to evaluate BMT sintering.

2.1.2 Ta_2O_5 powder as tantalum precursor

The commercially available Ta_2O_5 powder purchased (Advanced Materials, USA, 73R-0802, chemical purity 99.99%), with a particle size distribution with d50=5 μm, showed serious agglomeration and poor flowability when in suspension. In fact, this Ta_2O_5 powder was dispersed in various solvents (water, ethanol, isopropanol, etc.) by ultrasonic and magnetic stirring, but upon pumping using a peristaltic pump, the powder settled in the tubing under gravitational force and induced clogging during the feeding process. To improve the stability and flowability of the Ta precursors in the synthesis of BMT, two alternatives were considered: spheroidization (to prepare precursor S6) and nanocrystallization (to prepare precursors S2-S5). In the plasma-spheroidization process, a powder feeder was employed to axially feed the commercial Ta_2O_5 powder into a R.F. ICP torch (PL-50, Tekna Plasma Systems Inc., Sherbrooke, Québec, Canada), as described in Fig. 1 (Ref 17). Operating parameters are shown in Table 2. Besides, a commercial Ta metal powder (AEE Atlantic equipment engineers, USA, chemical purity 99.8%, 1~5 μm) was axially fed in the same R.F. ICP torch to produce

nanosized Ta_2O_5. The detailed parameters for the nanocrystallization process are also shown in Table 2.

2.1.3 Magnesium and barium solutions

Mg acetate $Mg(CH_3COO)_2•4H_2O$ (Fisher BioReagents, India, BP215-500), Ba acetate $Ba(CH_3COO)_2$ (Sigma-Aldrich, Germany, 32305), Mg nitrate $Mg(NO_3)_2•6H_2O$ (Alfa Aesar, America, 11564) and Ba nitrate $Ba(NO_3)_2$ (Sigma-Aldrich, Germany, 217571) were chosen as the acetate-based (S5) and nitrate-based (S2-S4, S6) precursors, respectively.

2.2 Preparation of BMT coating

Titanium alloy (Ti-6Al-4V) with a diameter of 12.6 mm and a thickness of 2 mm was selected as substrate. All the substrates were sand-blasted and cleaned by acetone and ethanol successively. The substrates were cooled from beneath, being in contact with the water-cooled substrate holder at the tip of the robotized arm, as shown in Fig. 2. The liquid precursors listed in Table1 were fed by a peristaltic pump to an atomizing injection probe (SDR792-02B1, Tekna Plasma Systems Inc., Sherbrooke, Quebec, Canada). To increase the plasma jet momentum towards the substrate, a 25 mm converging nozzle (Ref 12) was installed at the outlet of the torch. The plasma parameters used for coating deposition are shown in Table 3.

2.3 Material characterization

X-ray photoelectron spectroscopy (XPS) was used to evaluate the element loss after spraying. It was performed with a Kratos Axis Ultra spectrometer (Manchester, United-Kingdom) using a monochromatic Al Kα source (140W). The analyzer was operated in a constant energy mode, i.e. *PE* = 160 eV. The analyzed area was an oval of dimensions 300 x 700 µm. Data analysis was conducted using the Casa XPS software (version 2.3.18). Thermogravimetric / Differential Thermal Analysis (TG/DTA) (04042, Setaram, France) were applied to analyze the BMT formation process. Phase structure and microstructure were analyzed by X-ray Diffraction (XRD) (X'pert PRO, PHILIPS, Netherlands) and Scanning Electron Microscopy (SEM) (S-3000N, Hitachi, Japan), respectively.

3. Results and Discussion

3.1 Ta_2O_5 spheroidization and nanocrystallization

Figure 3a and 3b show the morphologies of the commercial Ta_2O_5 and Ta metal powders, while that of the spheroidized and nanocrystallized Ta_2O_5 powders are shown in Fig. 3c and 3d, respectively. When fed into the plasma, the agglomerated commercial Ta_2O_5 powder was molten and quenched (Ref 18) to form particles having a smooth spherical appearance with a diameter around 40 µm, as seen in Fig. 3c and Fig. 4c. In comparison, the Ta_2O_5 nanopowder produced is much smaller, with d10=77 nm, d50=120 nm and d90=193 nm, as seen in Fig. 3d and Fig. 4d. A typical R.F. ICP nanopowder production process starts with a metal that is heated up and evaporated by the plasma jet. The resulting metal vapors are then quickly quenched to induce

nucleation and to limit the particle growth to nanosizes (Ref 19). To evaporate a large amount of Ta metal during the nanocrystallization process, the plasma power was increased to 58 kW compared to 43 kW for spheroidization. Oxygen was introduced in the sheath gas to oxidize the Ta vapors and to form Ta_2O_5. The addition of He to the sheath gas increased the thermal conductivity and enhanced the heat transfer process towards the Ta particles. The XRD diffractograms for the spheroidized and the nanocrystallized Ta_2O_5 powders are shown in Fig. 5, the main phase structure being Ta_2O_5 for both. Still, a peak of Ta (38.47°) remained after the nanocrystallization process, but it could not be distinguished at a macroscale; the nanocrystallized Ta_2O_5 powder had a white colour.

3.2 Characterization of synthesized and post-calcined BMT powder

The furnace-synthesized BMT powder at 1400 °C for 2h corresponds to the complex perovskite BMT phase structure (ICDD card No. 04-014-7667, PDF+4 2018), as seen in Fig. 6a. The peak near 17.65°, as indicated by the club symbol, corresponds to the Miller index (100) which is the strongest peak produced by the superlattice. The strongest peak in the whole pattern is shared by the disordered BMT (110) and the ordered BMT (012). The ordering degree can be calculated according to Mastumoto's formula (Ref 20),

$$S = \sqrt{\frac{\left(I_{100} \ / \ I_{110,012}\right)_{obs}}{\left(I_{100} \ / \ I_{110,012}\right)_{order}}} \quad (1)$$

where "obs" means the observed intensity of reflection peak. Mastumoto et al. indicated that the fully ordered value of $(I_{100}/I_{110,012})_{order}$ is 8.3 %. Therefore, the furnace-

synthesized BMT powder has an intermediate phase, with an ordering degree of 24 %. The XRD profiles of synthesized BMT after post calcination at different temperatures are shown in Fig. 6b. The characteristic peak height of the ordered phase near 17.65° increases abruptly after calcination at 1400 °C. In addition, other superlattice diffraction peaks, originating from (111), (200), (112) and (103), become obvious above 1400 °C, as indicated by the red rectangles. The ordering degree fluctuates for calcination temperatures between 1100 °C and 1300 °C, and it increases sharply above 1400 °C (see Fig. 6c). Therefore, 1400 °C appears to be a threshold temperature for the ordering transition. This observation is similar to published results where a BMT structure refinement was carried (Ref 21).

Figure 7 shows the morphologies of the synthesized / pre-calcined and post-calcined BMT powders at different temperatures. The synthesized BMT shows sharp edges with small particles (Fig. 7a). After post-calcination at 1100 °C and 1200 °C, a similar microstructure with tiny particles and sharp edges is still observed (Fig. 7b, 7c). The sintering neck occurred after calcination at 1300 °C, while tiny particles disappeared and plate-shaped particles started to sinter around 1400 °C. Meanwhile, the porosity decreased. After a calcination at 1500 °C, grains grew up and began to touch each other; sintering was complete. Based on these sintering observations, BMT is predicted to be used in service at temperature up to 1300-1400 °C.

3.3 Phase decomposition

The coating prepared from suspension S1 and S2 (table2) were analyzed by XPS to estimate the elemental decomposition during spraying. The concentrations and Full width at half maximum (FWHM) of each element are shown in Table 4 and their corresponding positions are marked in Fig. 8. The elemental composition of synthesized BMT powder is used as the reference standard. The interference of carbon is unavoidable because of the air and surface contamination. The sample was mounted on a non-conductive tape and a charge neutralizer was used on all samples to compensate for the charging effect. Charge corrections were performed using the adventitious carbon peak set at 284.8 eV. Copper contamination is observed on the surface of the samples. It originates from the erosion of the plasma torch supersonic nozzle at high plasma power. The signal of carbon disappeared after etching with an argon ion gun. Since XPS provides semi-quantitative results, the ratios of the main elements are used to evaluate elemental losses during plasma spraying. The Mg/Ba ratio of as-synthesized BMT powder is 0.2, while it decreases to 0.1 in as-sprayed coatings from S1 and S2 precursors. The Mg/Ta ratio of 0.3 for the powder also decreases to 0.1 in both S1 and S2 conditions. Thus, in as-sprayed coatings from S1 and S2, the Mg:Ba and Mg:Ta ratios decreased to one half and one third the fed values, respectively. Losses of Ba (versus Ta) are also observed in plasma sprayed coatings. Due to its high vapor pressure, Mg tends to evaporate easily (859°C, 10 kPa; 1088°C, 100 kPa), compared to Ba (1413°C, 10 kPa; 1897°C, 100 kPa) and Ta (4666°C, 10 kPa; 5361°C, 100 kPa) (Ref 22). In summary, it can be estimated that little or no loss of Ta occurred.

In contrast, Mg was depleted by half or more, whereas Ba was mostly conserved during spraying.

The influence of the Mg amount in the precursors on the final BMT coating phase structure was further investigated. The precursors and corresponding plasma power used for that purpose were S1 (45 kW), S2 (53 kW), S3 (53 kW) and S4 (53 kW), as indicated in Table 1. With higher plasma powers (50 kW and 53kW), the as-sprayed coating from suspension S1 cracked frequently. Accordingly, a power of 45 kW was chosen to prepare the coating and pursue the analyses with S1. The XRD results are shown in Fig. 9. The as-sprayed coating prepared by precursor S1 contains the Mg-depleted phases consisting of orthorhombic $BaTa_2O_6$ and $Ba_3Ta_5O_{15}$. The presence of MgO confirms the decomposition of BMT powder at high temperature. The formation of Mg-depleted phases is attributed to the decomposition of BMT and to the preferential evaporation of MgO during spraying. Similarly, APS-sprayed BMT coatings also contain $Ba_3Ta_5O_{15}$ because of Mg oxide loss, which was verified by chemical analysis (Ref 7).

Due to losses of MgO and BaO, TaO_2 is left in the as-sprayed coating prepared by precursor S2. The Ta_2O_5 fed with the precursor does not appear on the diffractogram, which indicates that Ta_2O_5 probably decomposed in the plasma. Hexagonal $BaTa_2O_6$ also occurs in the coating produced from precursor S2. It is normally formed at high temperatures (between 1300-1900°C), compared to the orthorhombic phase which forms below 1150°C. The occurrence of orthorhombic $BaTa_2O_6$ in as-sprayed coating from precursor S1 is thus also attributed to the lower plasma power of 45 kW. Layden

et al. tried to prepare the hexagonal phase by cooling from the melt, but all the different phases of $Ba_2Ta_2O_6$ were observed, including the tetragonal structure (Ref 23). Since only two phases occurred in this work, further exploration is needed possibly discriminate all the phases. Still, it should be mentioned that tetragonal $BaTa_2O_6$ is isostructural with $Ba_3Ta_5O_{15}$, characterized by the tetragonal tungsten bronze (TTB) structure (Ref 24). These two phases are always hard to discriminate owing to nearly identical Bragg peak positions. In addition, the only ICDD card available for tetragonal $BaTa_2O_6$ (No. 00-050-1706) shows the Bragg peak positions up to a maximum of 50°. Accordingly, the confounded phases are identified as $Ba_3Ta_5O_{15}$ in this work.

The Mg-rich phase, $Mg_4Ta_2O_9$, exists in all coatings sprayed from suspension/solution precursors (S2, S3 and S4), as shown in Fig. 9. As such, the appearance of the Mg-rich phase cannot be solely attributed to an excess in Mg amount. Three kinds of oxides ($Mg_4Ta_2O_9$, $MgTa_2O_6$, $Mg_5Ta_4O_{15}$) exist in the binary-system of MgO-Ta_2O_5. In the bulk material, $Mg_4Ta_2O_9$ and $MgTa_2O_6$ co-exist over the range 900-1580 °C and stabilize to their respective melting temperature of 1830 °C and 1770 °C (Ref 25). Above 1100 °C, only $Mg_4Ta_2O_9$ exists during the vapor-solid reactions for MgO-Ta_2O_5 thin films preparation (Ref 26). This phenomenon is consistent with our working conditions, where the MgO vapor reacts with molten or semi-molten Ta_2O_5 powder.

3.4 Effect of heat treatment

The phase structure of BMT coatings obtained with different pre-heating, post-heating (blank plasma passes over the sample) and spraying distance was investigated using

precursor S5 with a plasma power of 53 kW. In preliminary works, lower plasma power and fast cooling led to incompletely reacted products ($BaCO_3$, Ta_2O_5 and MgO etc.) and a large amount of amorphous phase in the as-sprayed coatings. A similar phenomenon also occurred in other studies. For example, when injecting a suspension containing MnO_2 and $LaCl_3$, the as-sprayed coating showed a mixture of $LaMnO_{3.15}$, La_2O_3 and Mn_3O_4, while a plasma post-heating treatment promoted the complete reaction to form $LaMnO_3$ (Ref 27). Thus, a post-heating treatment was applied to promote the completion of the chemical reaction towards BMT and to further induce crystallization of as-sprayed coating. The XRD profiles are shown in Fig. 10. Prolonged pre-heating and/or post heat treatment resulted in an increase of the substrate temperature, which obviously affected the phase structure. From the top pattern to the third pattern (Fig. 10), the heating effect increases. As a result, the main peak (around 31.7°) of the secondary phase $Ba_3Ta_5O_{15}$ increases in step. The relative heights of this $Ba_3Ta_5O_{15}$ peak to the main peak of BMT around 30.8° are 57 %, 70 % and 91.3 %, respectively. It can thus be estimated that the crystallinity of $Ba_3Ta_5O_{15}$ increases. When positioning the substrate further away from the plasma torch (spray distances of 140 mm and 150 mm), the relative heights drop to 12.5 % and 8.3 %, respectively. When spraying BMT in APS conditions, other researchers showed that thermal cycling at 1339°C increased the crystallinity of $Ba_3Ta_5O_{15}$ (Ref 6). Kolodiazhnyi et al. considered $Ba_3Ta_5O_{15}$ as a high temperature phase that only forms above 1630°C and as Schottky defects which spread over the interface (Ref 28). It could explain why increasing the heat load (such as prolonging pre-heating times, adding post heat

treatments and using a shorter spray distance) resulted in an increasing level of crystallinity of $Ba_3Ta_5O_{15}$. On the other hand, the crystallinity of orthorhombic $BaTa_2O_6$ (main peak around 28.8°) decreased when increasing the heating effect. By bringing the substrate closer to the plasma torch from 150 mm to 140 mm, the relative height of $BaTa_2O_6$ drops down from 54 % to 19.4 % and the peaks broadened.

The formation process of BMT is not a one-step reaction. $BaTa_2O_6$ acts as an intermediate product formed before BMT or as a by-product of BMT, as seen in formula (2-5) (Ref 29),

$$BaCO_3 + Ta_2O_5 \rightarrow BaTa_2O_6 + CO_2 \quad (2)$$

$$BaTa_2O_6 + 3BaCO_3 \rightarrow Ba_4Ta_2O_9 + 3CO_2 \quad (3)$$

$$Ba_4Ta_2O_9 + 1/3MgO + O_2 \rightarrow Ba(Mg_{1/3}Ta_{2/3})O_3 + 1/3BaTa_2O_6 + 3BaO \quad (4)$$

$$BaTa_2O_6 + 1/3MgO \rightarrow Ba(Mg_{1/3}Ta_{2/3})O_3 + 1/3Ta_2O_5 \quad (5)$$

It can be estimated that the relation between $BaTa_2O_6$ and BMT is that of a competitive growth. Less energy is suitable for the formation of $BaTa_2O_6$. In fact according to the reaction kinetic, the activation energy for the formation of $BaTa_2O_6$ is 235.6 kJ/mol (Ref 30), compared to the value of 257 kJ/mol (Ref 31) for BMT. As a conclusion of this section, the best heating effect is that with a short spraying distance. Pre-heating and post heat-treatment rank second and third, respectively. In addition, to attenuate the secondary phases formation, the best parameter combination is a 140 mm spraying distance with 20 pre-heating plasma passes. These conditions are adopted for the remaining sections in this paper.

3.5 Precursor chemistry

The BMT coating phase structure and micro-structure are analyzed to investigate the effect of precursor chemistry (acetate-based and nitrate-based precursors). The phase structures of BMT coatings sprayed from acetate-based precursor (S5) and nitrate-based precursor (S4) are shown in Fig. 11 and Fig. 12, respectively. When increasing the plasma power, the relative intensity between orthorhombic $Ba_2Ta_2O_6$ and BMT main peaks decreases in Fig. 11, which supports the competitive growth mechanism. Unreacted initial Ta_2O_5 remains in as-sprayed coating at lower plasma power of 45 kW and 50 kW; relatively pure BMT is only obtained at 53 kW. In contrast, nitrate-based precursors resulted in coatings with a dominant BMT phase starting from 45 kW. A power of 50 kW is enough to deposit relative pure BMT coatings. It should be mentioned that the $BaTa_2O_6$ phases can be fully eliminated when using nitrate-based precursors, as shown in Fig. 12.

The difference in reaction processes between nitrate-based and acetate-based precursors can be explained by TG-DTA curves, as seen in Fig. 13. The first weight loss plateau of acetate-based precursors occurs at 400°C and stops at 500°C, which corresponds to the decomposition of Ba acetate, as seen in formula (6). This decomposition is accompanied by an exothermic peak of large amplitude around 450°C.

$$Ba(CH_3COO)_2 \rightarrow BaCO_3 + (CH_3)_2CO \quad (6)$$

Experiments with pure barium acetate (doesn't show in this paper) under the same TG-DTA conditions indicated that $BaCO_3$ decomposes and releases CO_2 from 800°C up

until the test limit set at 1400 °C. The decomposition speed reaches the highest speed at 1200 °C. However, for the precursor S5, this decomposition occurs from 800 °C and stops at 1100 °C, illustrating the BMT synthesis reaction and indicating that the reaction with Ta_2O_5 and MgO promoted the decomposition process of $BaCO_3$. The decomposition of $Mg(CH_3COO)_2$ occurs in one step process (Ref 32). On the other hand, the decomposition process of $Ba(NO_3)_2$ is relatively simple from 400°C to 700°C and can be expressed using a simplified formula (7).

$$2Ba(NO_3)_2 \rightarrow 2BaO + 4NO_2 + O_2 \quad (7)$$

According to the DTA curve, an endothermic peak occurs at 650°C with nitrate-based precursors; this peak is attributed to the formation of BMT. On the contrary, BMT is formed gradually at 800°C (endothermic peak) while continuously releasing CO_2 from 800°C to 1100°C with acetate-based precursors. This result is similar to the conventional solid-state synthesis method which uses $BaCO_3$, Ta_2O_5 and MgO powders (Ref 33). It can explain why nitrate-based precursors resulted in BMT dominant coatings at 45 kW and relatively pure BMT coatings at 50 kW.

The diverse reaction processes also lead to differences in splat morphologies and coating deposition rate, as seen in SEM images (secondary electron) in Fig. 14. Coatings prepared from acetate-based precursors (Fig. 14a) show an irregular, porous and cauliflower-like morphology with a lot of small re-solidified particles and tiny molten droplets sticking to the big splat surface. The sizes of these tiny droplets are distributed from 0.5 μm to 2 μm. Coatings prepared from nitrate-based precursors (Fig. 14b) have a much more uniform morphology made of well molten splats and possess a

good bonding. Sivakumar et al. investigated the effect of precursor chemistry (aluminum nitrate and acetic acid modified aluminum acetate) on splat formation during SPPS. Due to the substantial heat of combustion of acetic acid and to the exothermic reactions of carbonaceous species, the resulting microstructure from the acetic acid modified aluminum acetate showed a significant amount of fine spherical particles, even at lower plasma power (Ref 34). A similar argument could explain the presence of tiny molten droplets on the big splat surface, as observed in Fig. 14a. Organic solutes such as acetate-based precursors are interesting choices to prepare some oxide coatings such as zirconia (Ref 35) and alumina (Ref 34) because of their exothermal reactions. For some other oxides, nitrate-based precursors are preferable to form oxides, such as BaO (in this work) and Y_2O_3 (Ref 36). Indeed, Y_2O_3 forms at a higher temperature (650°C) when using yttrium acetate compared to yttrium nitrate (450°C).

Another reason that could lead to the fine droplets (Fig. 14a) is the release of CO_2 from acetate-based precursors which breaks the big droplets into tiny ones. This phenomenon can be regarded as a secondary explosion, which is similar to the "secondary atomization" known to happen in SPPS (Ref 11). When the plasma jet (gas flow) hits the substrate, its direction changes from perpendicular to parallel to the substrate surface. The smaller droplets mingled in the gas/plasma jet have a small Stokes number and are sensitive to changes in gas/plasma direction (Ref 37). Oberste-Berghaus et al. proved this phenomenon using numerical modeling. Near the substrate, tiny droplets (<1 μm) will follow the gas flow, parallel to substrate surface (Ref 38). When the drag

force overcomes the adhesion force, tiny droplets cannot deposit on substrate (Ref 39). This can explain the difference in deposited coating thickness as shown in Fig. 14c and 14d, after the same number of spraying loops (46 loops). The coating deposition rate from nitrate precursor is 1.56 times higher than that from acetate precursors. Still, the maximum deposition rate was only 0.26 μm per pass, mainly because of the small feed rate and low precursor concentration required to avoid the obstruction of the injection probe. Further optimization will be needed to produce BMT TBCs at a larger scale.

3.6 Effect of initial Ta_2O_5 particle size

Since helium used in nanocrystallization comes with a high price tag, the spheroidization process was considered as an alternative to synthesize Ta_2O_5 powders with good stability and flowability when in suspension. Said spheroidized powders were used in the combination of precursor S6 (Table 1). The phase structures of BMT coatings sprayed from S6 precursors are shown in Fig. 15. TaO_2, another Ta oxide and MgO were found in as-sprayed coating for each plasma power tested. These oxides approximately correspond to the initial reactants. The energy required to fully melt a spherical particle is shown in equation (8) (Ref 40):

$$Q=1/6\ \pi d^3\rho \quad [c_p(T_m-T_0)+H_m] \tag{8}$$

For the same material and conditions, the density ρ, specific heat c_p, melting temperature T_m, room temperature T_0 and latent heat of fusion H_m are considered as constant. Accordingly, the particle diameter d becomes the only variable determining the required energy. The particle size of spheroidized T_2O_5 is over 100 times larger than

that of nanocrystallized particles. As such, spheroidized Ta_2O_5 requires much more energy to fully melt and to react with other precursors. According to the evaporation results for Ba (see the Ta/Ba ratio in Table 4), Ba evaporation is more important for nitrate-based precursors (S2) compared to a pure BMT suspension (S1). Therefore, unmolten spheroidized Ta_2O_5 will reduce the reaction rate with Ba precursors, which could worsen the evaporation of Ba. The occurrence of $BaCO_3$ at 45 kW may result from the reaction between BaO and CO_2, which came from the decomposed ethanol. The transition from Ba_3TaO_{15} and $BaTa_2O_6$ at 50 kW to $Ba_4Ta_2O_9$ at 53 kW can be described as formula (9).

$$Ba_3TaO_{15} + BaTa_2O_6 \rightarrow Ba_4Ta_2O_9 + 2Ta_2O_5 + TaO_2 \quad (9)$$

This reaction contains the different Ta oxides as by-products.

The cross-sectional image of coating sprayed by precursor S6 with plasma power of 50kW is shown in Fig. 16. The black dots within the rectangle correspond to MgO, while Ta oxides are formed at the interface between the substrate and the coating (black arrows). These phenomenon is identical with the XRD results in Fig. 15.

To summarize, spheroidized Ta_2O_5 is an interesting raw material to synthesize BMT in hybrid SPS/SPPS. Still, it needs higher plasma power and slows the reaction. As a result, it intensifies the evaporation and loss of Ba.

4. Conclusions

In the proposed hybrid SPS/SPPS process, $Ba(Mg_{1/3}Ta_{2/3})O_3$ formation and Mg evaporation happened simultaneously, together with the formation of four secondary

phases: three Mg-depleted phases ($BaTa_2O_6$, $Ba_3Ta_5O_{15}$ and $Ba_4Ta_2O_9$) and one Mg-rich phase ($Mg_4Ta_2O_9$). $BaTa_2O_6$ grew competitively with BMT during the reaction. Decomposition of BMT during plasma spraying and Schottky defects resulting from higher substrate temperatures both contributed to the formation of $Ba_3Ta_5O_{15}$. $Mg_4Ta_2O_9$ was systematically observed, even in coatings sprayed from stoichiometric precursors (without Mg excess), which illustrates the complex reaction processes.

The detailed comparisons of the deposited phases from different precursors and spray conditions can be summarized as:

1. As-sprayed coatings prepared by SPS (BMT powder suspension) contained Mg-depleted phases, illustrating the preferential Mg losses during plasma spraying. In comparison, as-sprayed coating from a suspension of nanosized Ta_2O_5 powder in a solution of Ba and Mg salts showed a Mg-rich phase in addition to the Mg-depleted phases.
2. Precursor chemistry played a key role in BMT synthesis and coating preparation. Orthorhombic $BaTa_2O_6$ only occurs in coating sprayed from acetate-based precursor. Coating sprayed from nitrate-based precursor can avoid the formation of $BaTa_2O_6$ of any phase structure when using twice the stoichiometric Mg amount. Due to their complex decomposition and reaction process, acetate-based precursors resulted in coatings with lower deposition rate and complex secondary phases. In opposition, nitrate-based precursors contributed to obtaining thicker coatings with higher purity at lower plasma power (50 kW).

3. Using a large spheroidized Ta_2O_5 powder decreased the reaction rate. It resulted in incomplete reactions and intermediate products (e.g. Mg oxide, Ta oxide) were found in the as-sprayed coatings for all conditions. In contrary, nanocrystallized Ta_2O_5 powders made the complete reaction towards BMT much easier.

To obtain a relatively pure BMT coating, it was shown that twice the Mg stoichiometric amount and a power of 50 kW provided the best results when using nanocrystallized Ta_2O_5 as a tantalum precursor and nitrated-based salts as barium and magnesium precursors. Still, the low deposition rate observed needs to be improved by increasing the feed rate and the precursor concentration, among other parameters.

Acknowledgments The financial support by the Fonds de recherche du Québec - Nature et technologies (FRQNT), the Natural Sciences and Engineering Research Council of Canada (NSERC), and Université de Sherbrooke is gratefully acknowledged. The authors also appreciate the technical support from Kossi Béré.

References

1. N.P. Padture, M. Gell, and E.H. Jordan, Thermal barrier coatings for gas-turbine engine applications, *Science*, 2002, **296**(5566), p 280-284
2. X.Q. Cao, R. Vassen, and D. Stoever, Ceramic materials for thermal barrier coatings, *J. Eur. Ceram. Soc.*, 2004, **24**(1), p 1-10
3. R. Guo, A.S. Bhalla, and L.E. Cross, $Ba(Mg_{1/3}Ta_{2/3})O_3$ Single crystal fiber grown by the laser-heated pedestal growth technique., *J. Appl. Phys.*, 1994, **75**(9), p 4704-4708
4. C. Jinga, E. Andronescu, S. Jinga, A. Ioachim, L. Nedelcu, and M. Toacsan, Synthesis and characterization of doped Ba $(Mg_{1/3}Ta_{2/3})$ O_3 ceramics, *J. Optoelectron. Adv. M.*, 2010, **12**(2), p 282-287
5. M.O. Jarligo, D.E. Mack, R. Vassen, and D. Stover, Application of Plasma-Sprayed Complex Perovskites as Thermal Barrier Coatings, *J. Therm. Spray Technol.*, 2009, **18**(2), p 187-193
6. M.O. Jarligo, D.E. Mack, G. Mauer, R. Vassen, and D. Stoever, Atmospheric Plasma Spraying of High Melting Temperature Complex Perovskites for TBC Application, *J. Therm. Spray Technol.*, 2010, **19**(1-2), p 303-310
7. M.O. Jarligo, G. Mauer, D. Sebold, D.E. Mack, R. Vassen, and D. Stoever, Decomposition of $Ba(Mg_{1/3}Ta_{2/3})O_3$ perovskite during atmospheric plasma spraying, *Surf. Coat. Tech.*, 2012, **206**(8-9), p 2515-2520
8. F. Gitzhofer, E. Bouyer, and M.I. Boulos, Suspension plasma spray, Patent US5609921A, 1997
9. E.H. Jordan, C. Jiang, and M. Gell, The Solution Precursor Plasma Spray (SPPS) process: A Review with Energy Considerations, *J. Therm. Spray Technol.*, 2015, **24**(7), p 1153-1165
10. A. Ganvir, C. Kumara, M. Gupta, and P. Nylen, Thermal Conductivity in Suspension Sprayed Thermal Barrier Coatings: Modeling and Experiments, *J. Therm. Spray Technol.*, 2017, **26**(1), p 71-82
11. É. Darthout, A. Quet, N. Braidy, and F. Gitzhofer, Lu_2O_3-SiO_2-ZrO_2 Coatings for Environmental Barrier Application by Solution Precursor Plasma Spraying and

Influence of Precursor Chemistry, *J. Therm. Spray Technol.*, 2013, **23**(3), p 325-332

12. É. Darthout, G. Laduye, and F. Gitzhofer, Processing Parameter Effects and Thermal Properties of $Y_2Si_2O_7$ Nanostructured Environmental Barrier Coatings Synthesized by Solution Precursor Induction Plasma Spraying, *J. Therm. Spray Technol.*, 2016, **25**(7), p 1264-1279
13. A. Guignard, G. Mauer, R. Vassen, and D. Stoever, Deposition and Characteristics of Submicrometer-Structured Thermal Barrier Coatings by Suspension Plasma Spraying, *J. Therm. Spray Technol.*, 2012, **21**(3-4), p 416-424
14. P. Fauchais, M. Vardelle, A. Vardelle, and S. Goutier, What Do We Know, What are the Current Limitations of Suspension Plasma Spraying? , *J. Therm. Spray Technol.*, 2015, **24**(7), p 1120-1129
15. L. Jia and F. Gitzhofer, Induction plasma synthesis of nano-structured SOFCs electrolyte using solution and suspension plasma spraying: a comparative study, *J. Therm. Spray Technol.*, 2010, **19**(3), p 566-574
16. M. Marr, J. Kuhn, C. Metcalfe, J. Harris, and O. Kesler, Electrochemical performance of solid oxide fuel cells having electrolytes made by suspension and solution precursor plasma spraying, *J. Power Sources*, 2014, **245**, p 398-405
17. K. Major, J. Veilleux, and G. Brisard, Lithium iron phosphate powders and coatings obtained by means of inductively coupled thermal plasma, *J. Therm. Spray Technol.*, 2016, **25**(1-2), p 357-364
18. H. Hou, X. Ning, Q. Wang, Y. Liu, and Y. Liu, Anti-ablation behavior of air plasma-sprayed Mo(Si, $Al)_2$ coating, *Surf. Coat. Tech.*, 2015, **274**, p 60-67
19. J. Guo, X. Fan, R. Dolbec, and S. Xue, J. Jurewicz and M. Boulos, Development of Nanopowder Synthesis Using Induction Plasma, *Plasma Sci. Technol.*, 2010, **12**(2), p 188-199
20. K. Matsumoto, T. Hiuga, K. Takada, and H. Ichimura, Ba $(Mg_{1/3}Ta_{2/3})O_3$ ceramics with ultra-low loss at microwave frequencies, *Sixth IEEE International Symposium on Applications of Ferroelectrics*, 1986, IEEE, New York, pp 118-121

21. S. Janaswamy, G. Sreenivasa Murthy, E.D. Dias, V.R.K. Murthy, Structural analysis of $BaMg_{1/3}(Ta,Nb)_{2/3}O_3$ ceramics, *Mater. Lett.,* 2002, **55**(6), p 414-419
22. D. R. Lide (ed), *CRC Handbook of Chemistry and Physics, 84the Edition.* Section 6: Fluid Propertues: vapor pressure, CRC press. Boca Raton, Florida, 2003.
23. G.K. Layden, Polymorphism of $BaTa_2O_6$, *Mater. Res. Bull.*, 1967, **2**(5), p 533-539
24. T. Kolodiazhnyi, A.A. Belik, T.C. Ozawa, and E. Takayama-Muromachi, Phase equilibria in the BaO–MgO–Ta_2O_5 system, *J. Mater. Chem.*, 2009, **19**(43), p 8212-8215
25. Y. Baskin, and D.C. Schell, Phase Studies in the Binary System MgO–Ta_2O_5, *J. Am. Ceram. Soc.*, 1963, **46**(4), p 174-177
26. D. Sun, S. Senz, and D. Hesse, Topotaxial formation of $Mg_4Ta_2O_9$ and $MgTa_2O_6$ thin films by vapour-solid reactions on MgO (001) crystals, *J. Eur. Ceram. Soc.*, 2004, **24**(8), p 2453-2463
27. G. Schiller, M. Muller, and F. Gitzhofer, Preparation of Perovskite Powders and Coatings by Radio Frequency Suspension Plasma Spraying, *J. Therm. Spray Technol.*, 1999, **8**(3), p 389-392
28. T.V. Kolodiazhnyi, A. Petric, G.P. Johari, and A.G. Belous, Effect of preparation conditions on cation ordering and dielectric properties of $Ba(Mg_{1/3}Ta_{2/3})O_3$ ceramics, *J. Eur. Ceram. Soc.*, 2002, **22**(12), p 2013-2021
29. Y. Fang, A. Hu, S. Ouyang, and J.J. Oh, The effect of calcination on the microwave dielectric properties of Ba $(Mg_{1/3}Ta_{2/3})O_3$, *J. Eur. Ceram. Soc.*, 2001, **21**(15), p 2745-2750
30. Y. Fang, A. Hu, Y. Gu, and Y.-J. Oh, Synthesis of $Ba(Mg_{1/3}Ta_{2/3})O_3$ microwave dielectrics by solid state processing, *J. Eur. Ceram. Soc.*, 2003, **23**(14), p 2497-2502
31. C.H. Lu and C.C. Tsai, Reaction kinetics, sintering characteristics, and ordering behavior of microwave dielectrics: Barium magnesium tantalate, *J. Mater. Res.*, 1996, **11**(5), p 1219-1227
32. M. Afzal, P. Butt, and H. Ahmad, Kinetics of thermal decomposition of metal acetates, *J. Therm. Anal. Calorim.*, 1991, **37**(5), p 1015-1023

33. K.P. Surendran, P.C.R. Varma, and M.R. Varma, Solid state and solution synthesis of $Ba(Mg_{1/3}Ta_{2/3})O_3$: A comparative study, *Mater. Res. Bull.*, 2007, **42**(10), p 1831-1844

34. G. Sivakumar, M. Ramakrishna, R.O. Dusane, and S.V. Joshi, Effect of SPPS Process Parameters on In-Flight Particle Generation and Splat Formation to Achieve Pure α-Al_2O_3 Coatings, *J. Therm. Spray Technol.*, 2015, **24**(7), p 1221-1234

35. G. Sivakumar, R.O. Dusane, and S.V. Joshi, In situ Particle Generation and Splat Formation During Solution Precursor Plasma Spraying of Yttria-Stabilized Zirconia Coatings, *J. Am. Ceram. Soc.*, 2011, **94**(12), p 4191-4199

36. H.M. Ismail and G.A.M. Hussein, Texture properties of yttrium oxides generated from different inorganic precursors, *Powder technol.*, 1996, **87**(1), p 87-92

37. P. Sokołowski, S. Kozerski, L. Pawłowski, and A. Ambroziak, The key process parameters influencing formation of columnar microstructure in suspension plasma sprayed zirconia coatings, *Surf. Coat. Tech.*, 2014, **260**, p 97-106

38. J.Oberste Berghaus, S. Bouaricha, J.G. Legoux, and C. Moreau, Injection Conditions and In-Flight Particle States in Suspension Plasma Spraying of Alumina and Zirconia Nano-Ceramics, *Proceedings of the International Thermal Spray Conference*, C. Berndt and E. Lugsheider, Ed., May 2-4, 2005 (Basel Switzerland), ASM Internationa, 2005

39. X. Chen., S. Kuroda, T. Ohnuki, H. Araki, M. Watanabe, and Y. Sakka, Effects of Processing Parameters on the Deposition of Yttria Partially Stabilized Zirconia Coating During Suspension Plasma Spray, *J. Am. Ceram. Soc.*, 2016, **99**(11), p 3546-3555

40. X.L. Jiang and M. Boulos, Induction plasma spheroidization of tungsten and molybdenum powders, *Trans. Nonferr. Met. Soc. China*, 2006, **16**(1), p 13-17

Figures

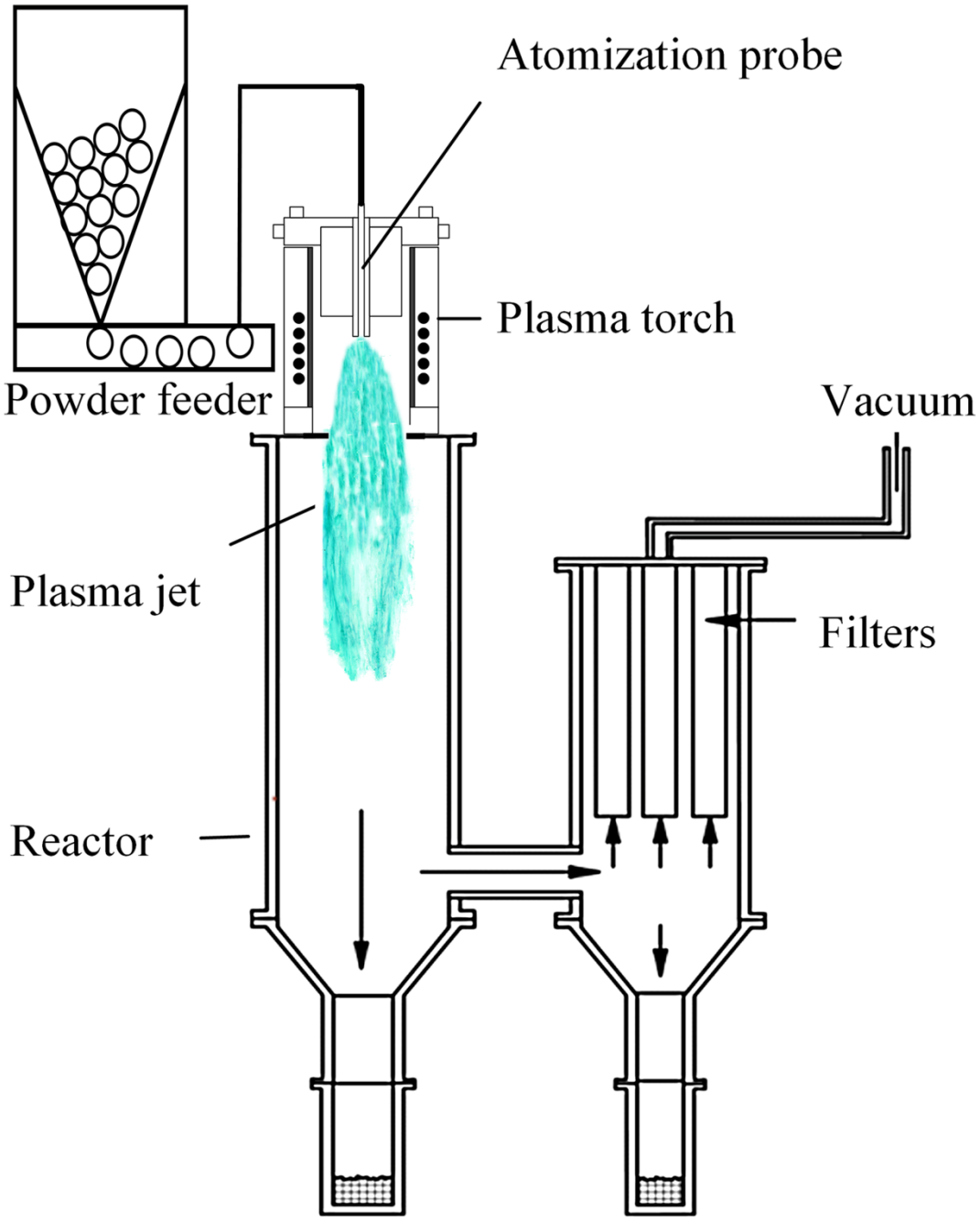

Fig. 1 Schematic illustration of induction plasma reactor with solid-state powder feeder for the spheroidization and nanocrystallization process.

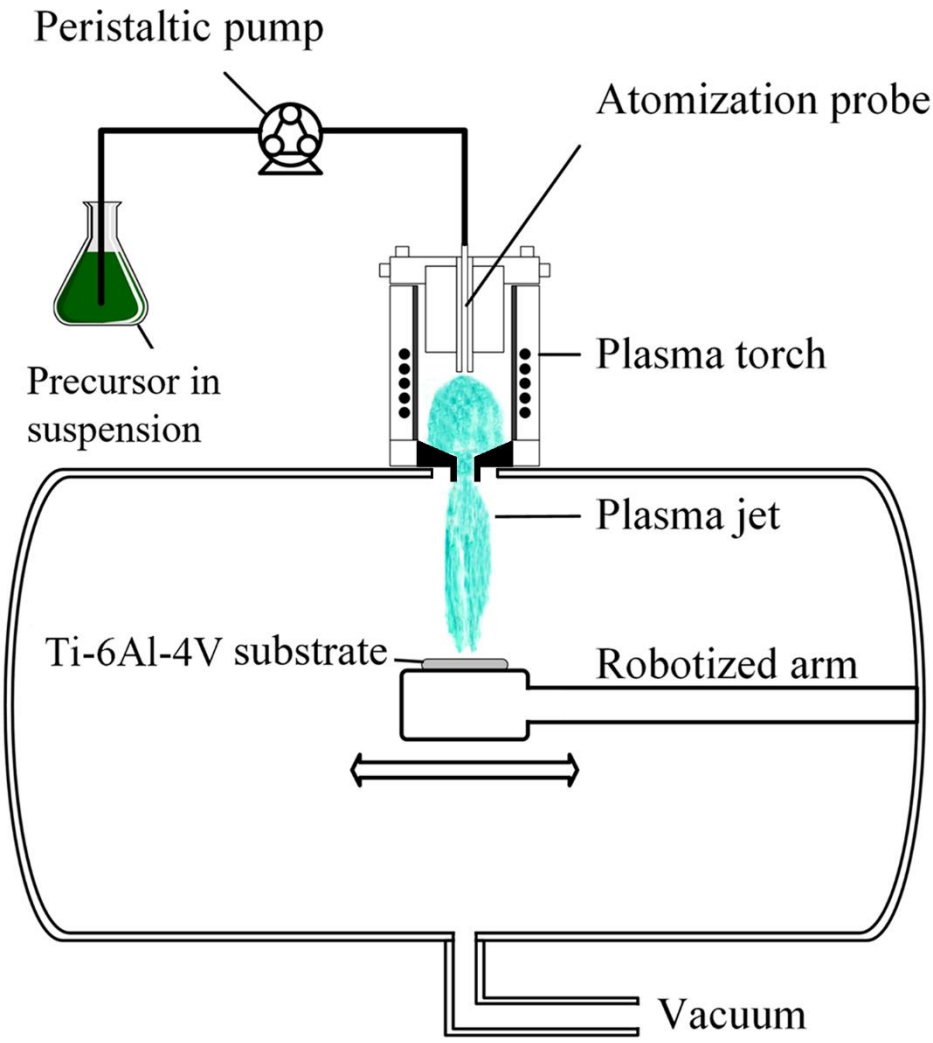

Fig. 2 Schematic illustration of induction plasma reactor for BMT coating deposition.

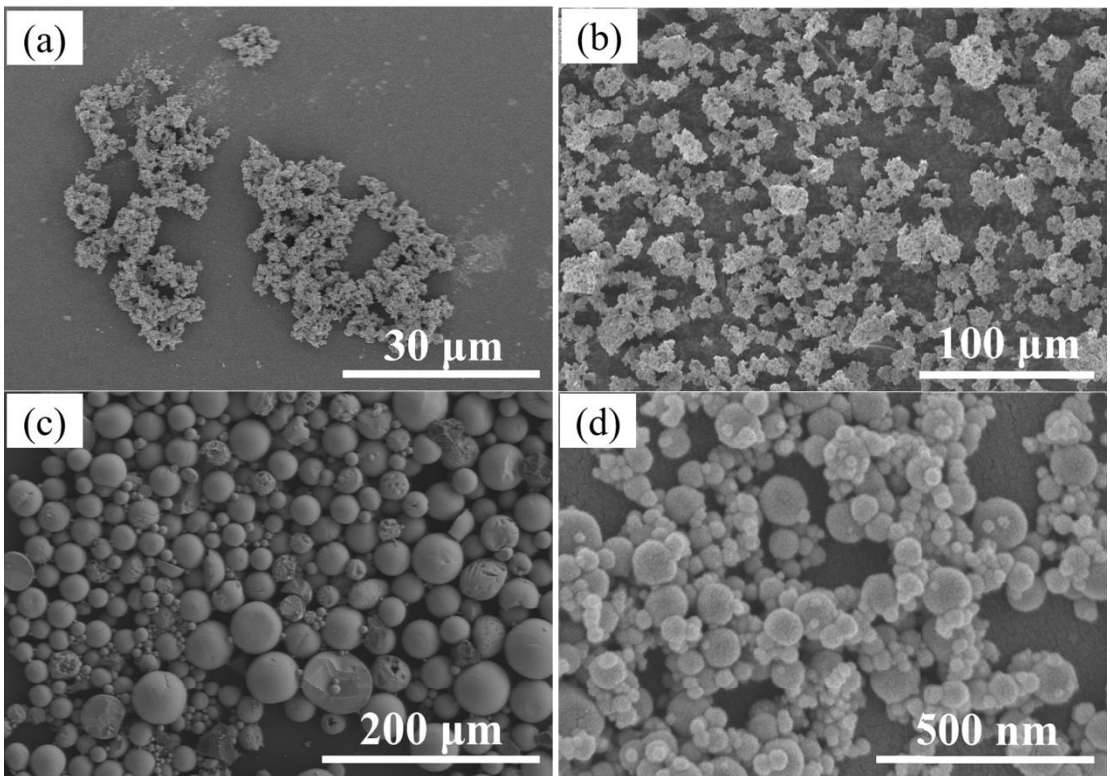

Fig. 3 Morphologies of particles (a) commercial Ta_2O_5, (b) commercial Ta metal, (c) plasma-spheroidized Ta_2O_5 and (c) plasma-nanocrystallized Ta_2O_5.

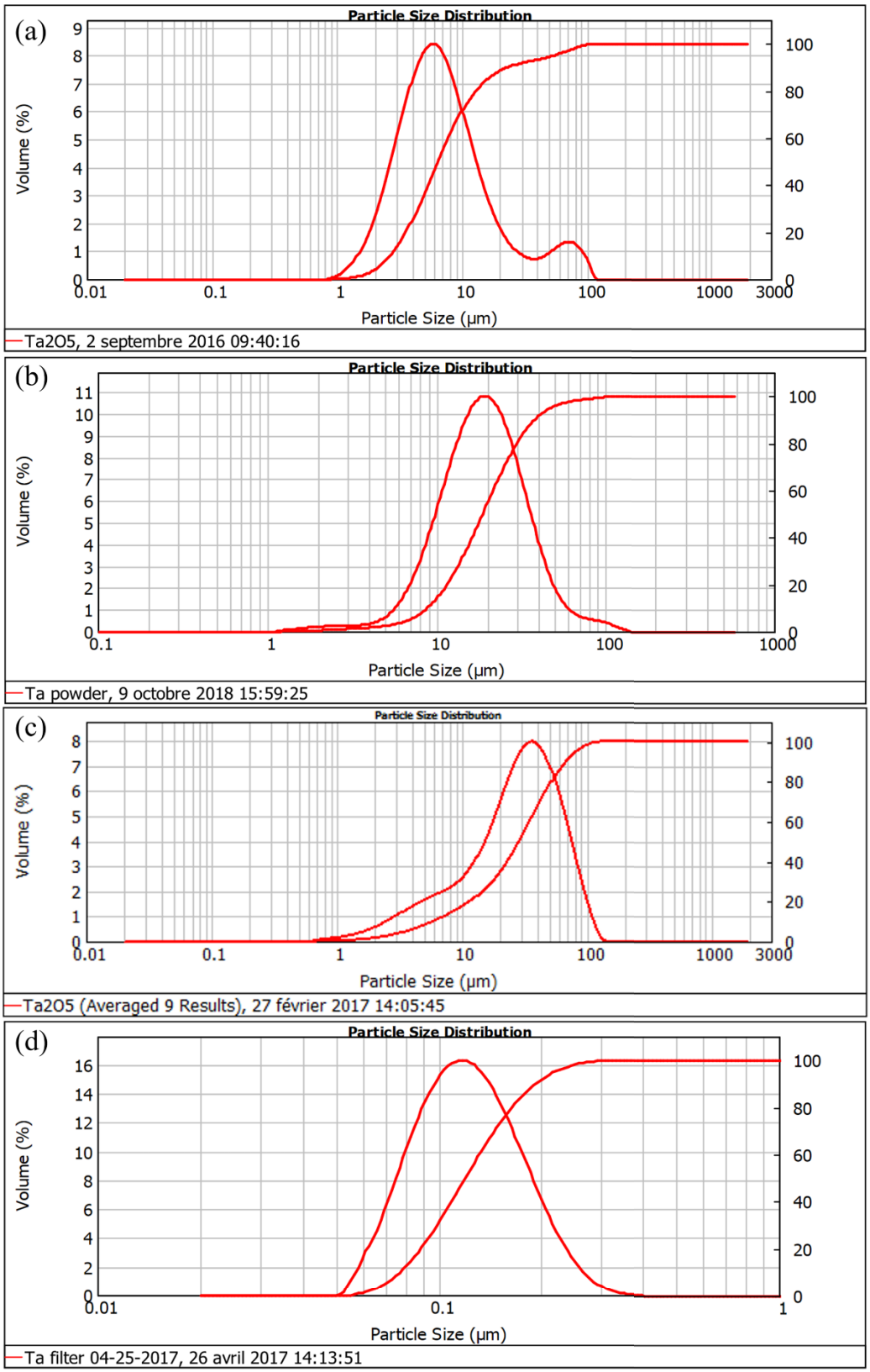

Fig. 4 Particle size distribution of (a) commercial Ta_2O_5, (b) commercial Ta metal, (c) plasma-spheroidized Ta_2O_5 and (c) plasma-nanocrystallized Ta_2O_5.

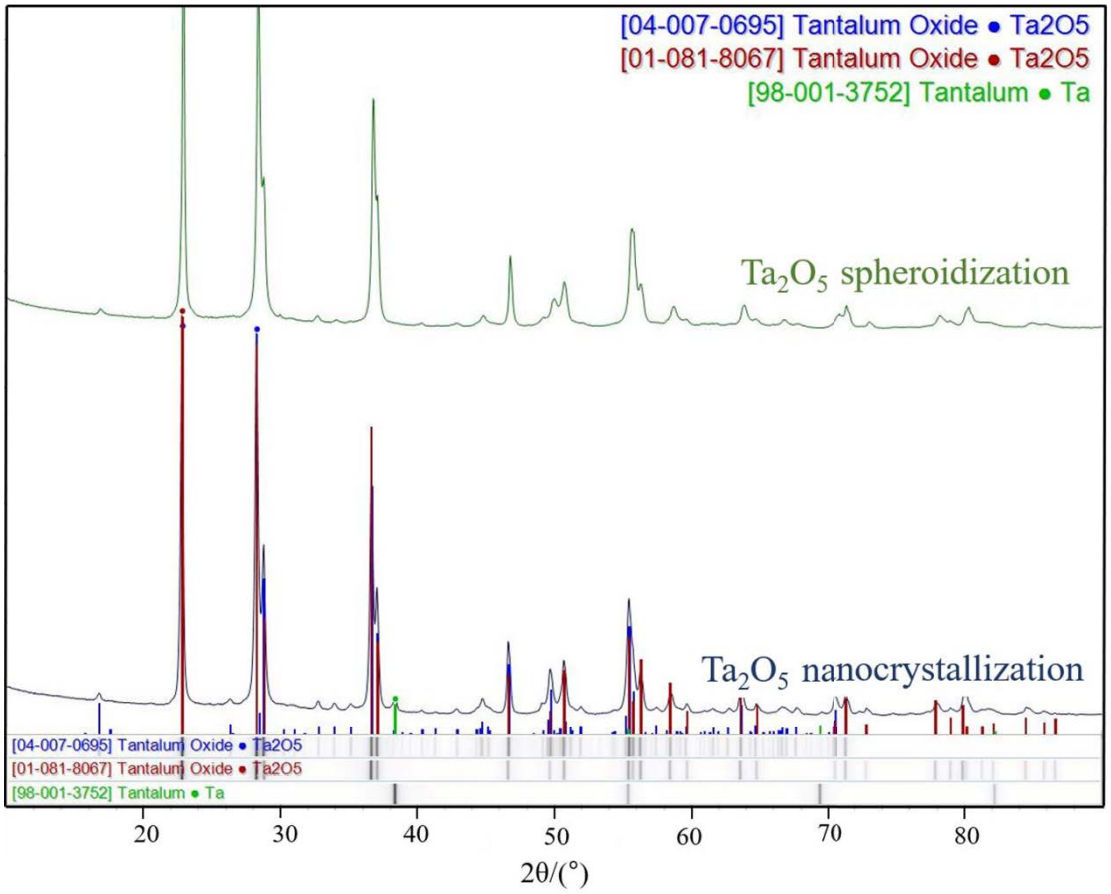

Fig. 5 X-ray diffractograms of plasma-nanocrystallized and plasma-spheroidized Ta_2O_5.

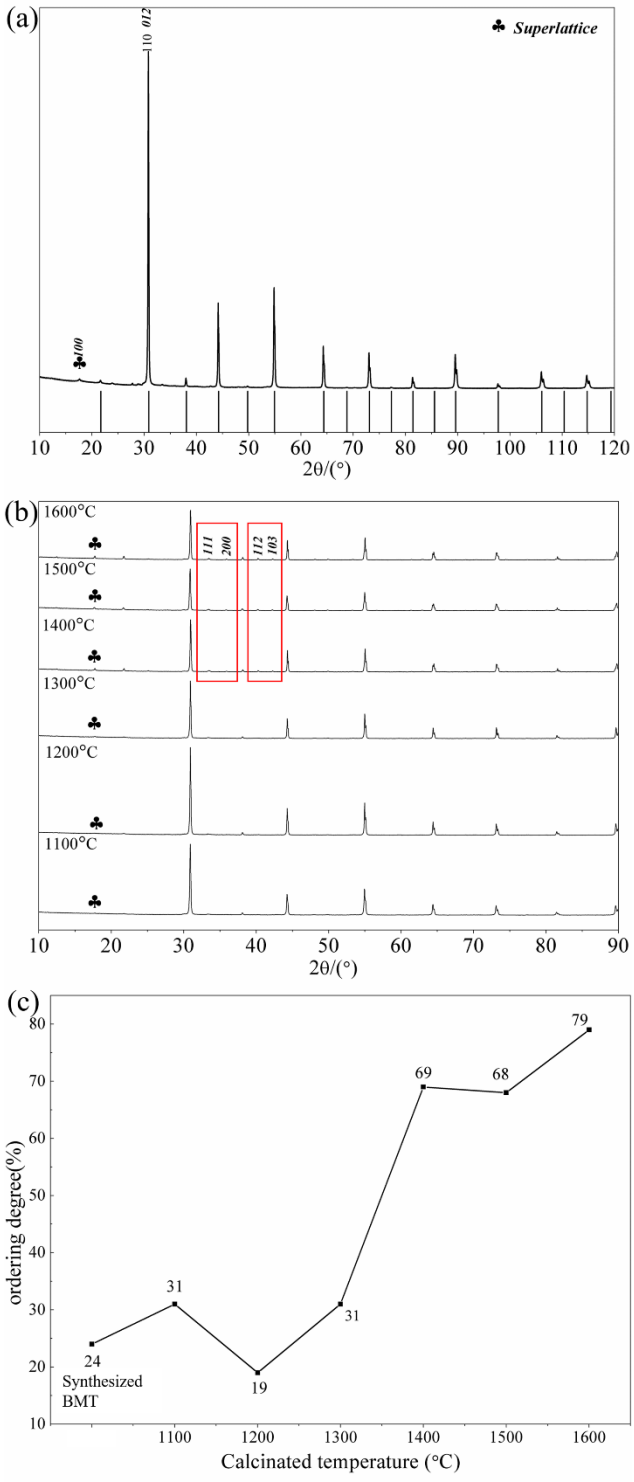

Fig. 6 X-ray diffractograms of (a) the as-synthesized BMT powder (vertical bars represent the positions of the cubic BMT phase reflection peaks from ICDD card No. 04-014-7667) and (b) after 2h post-calcination at different temperatures. The ordering degree of each powder is illustrated in (c).

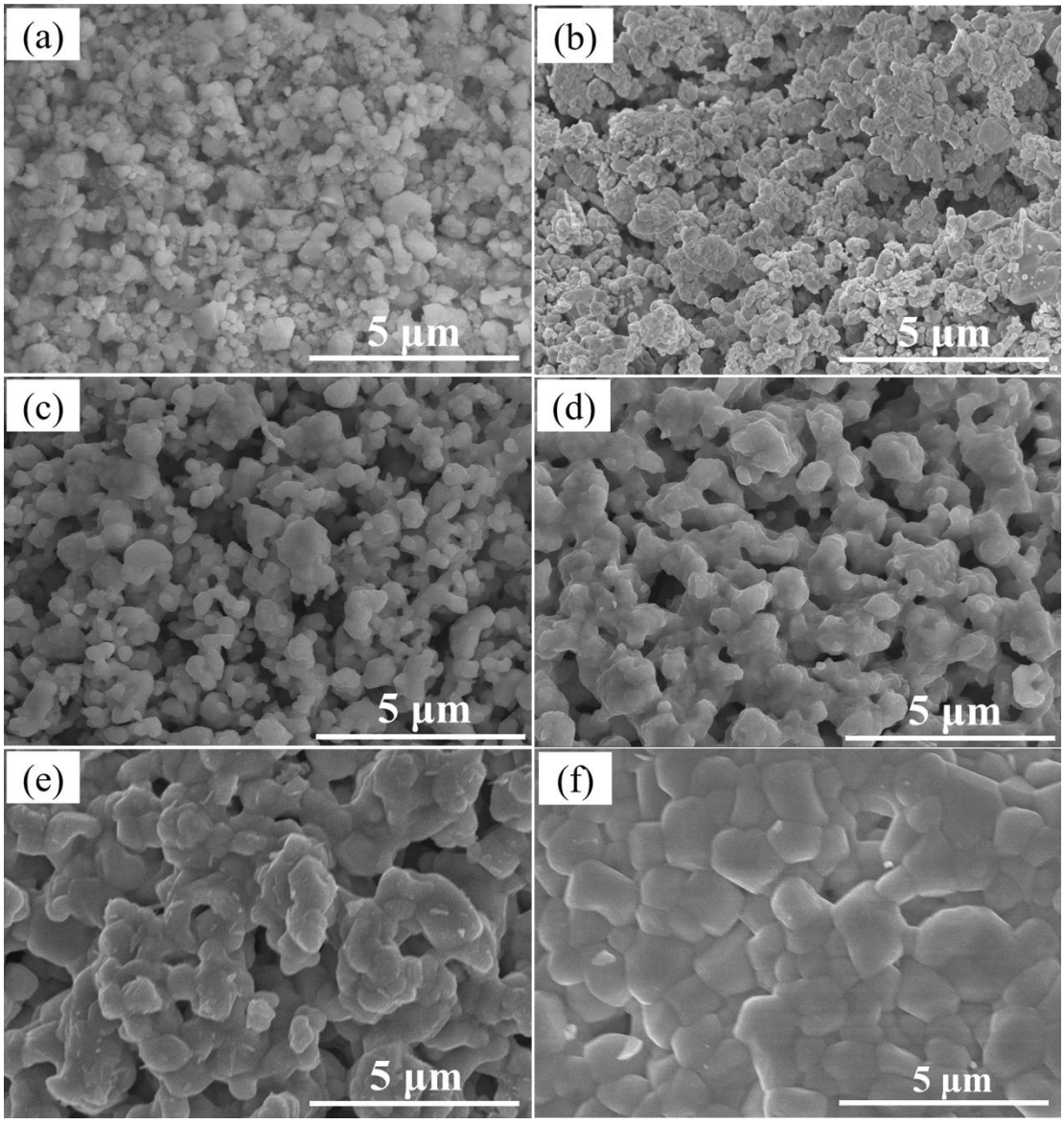

Fig. 7 Morphologies of synthesized BMT powder (a) and after 2h post-calcination at different temperatures (b) 1100 °C, (c) 1200 °C, (d) 1300 °C, (e) 1400 °C and (f) 1500 °C.

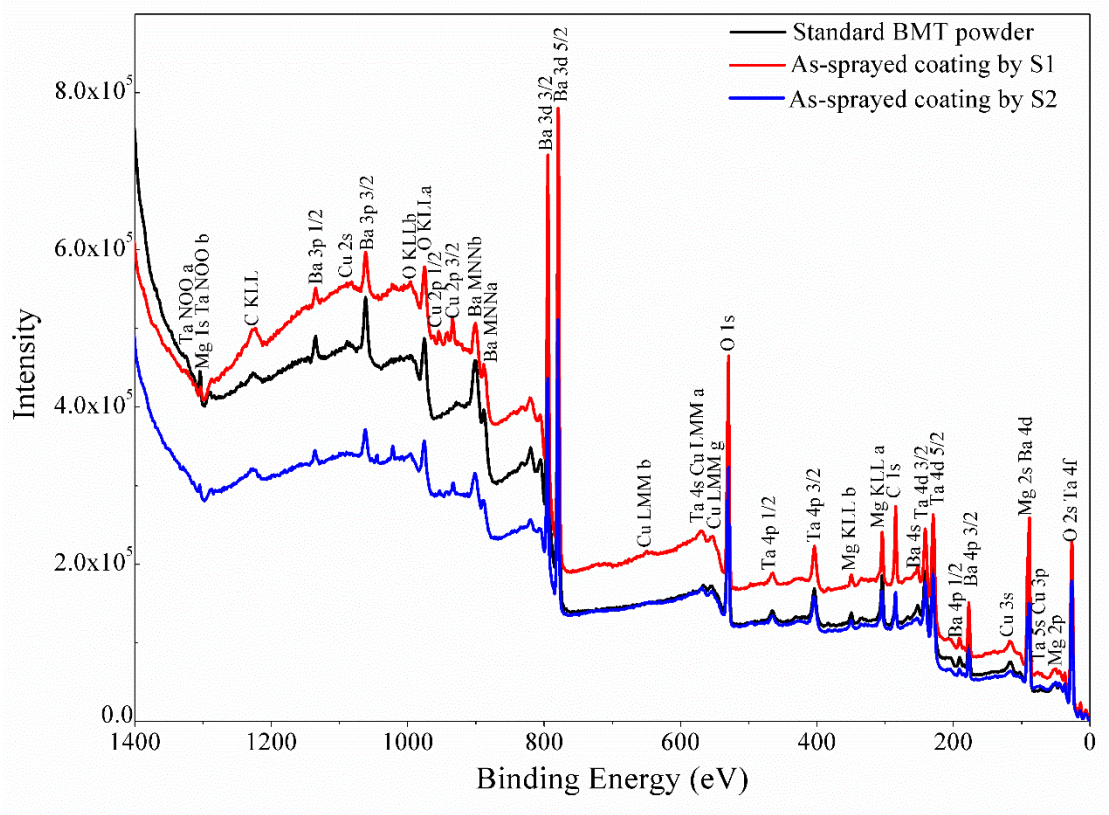

Fig. 8 General XPS spectra for the synthesized BMT powder (black), as-sprayed coating prepared by S1 (red) and by S2 (blue).

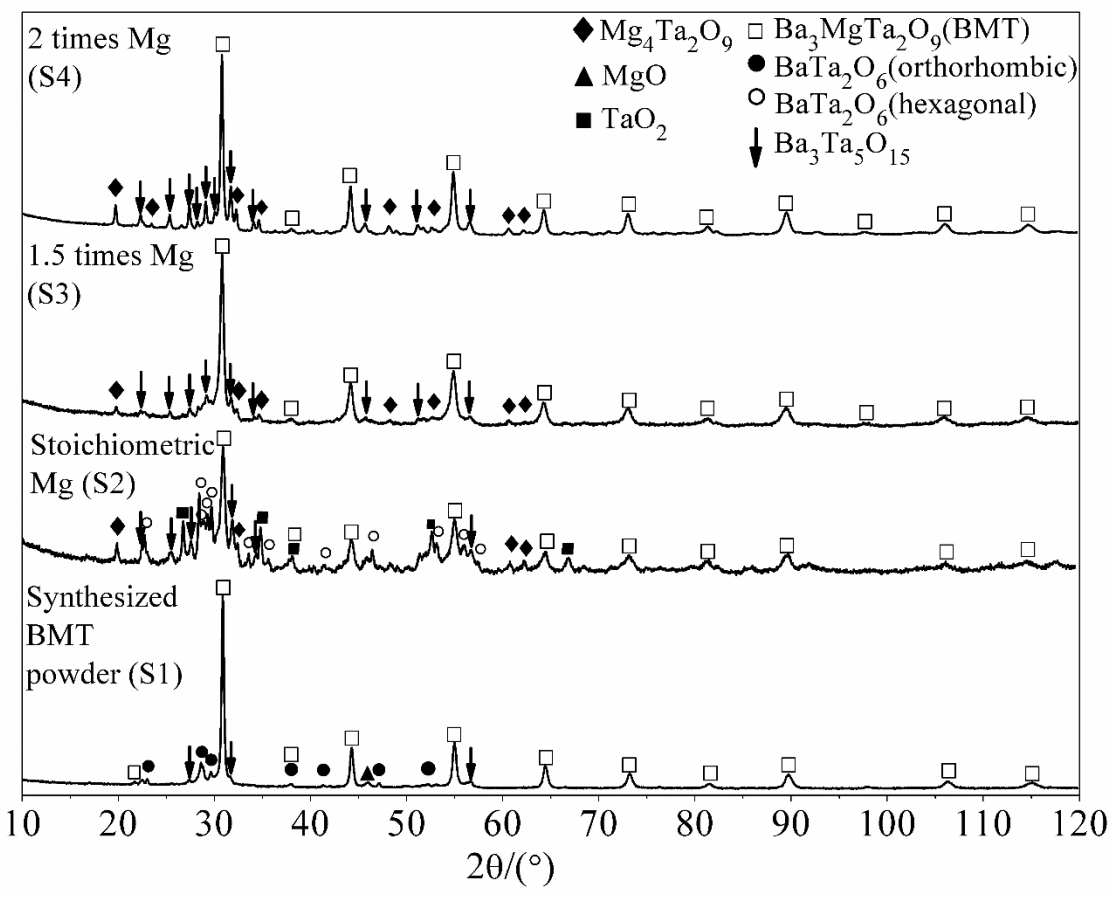

Fig. 9 X-ray diffractograms of as-sprayed coatings prepared by S1 (45 kW), S2 (53 kW), S3 (53 kW) and S4 (53 kW) precursors, which contained different initial amounts of Mg.

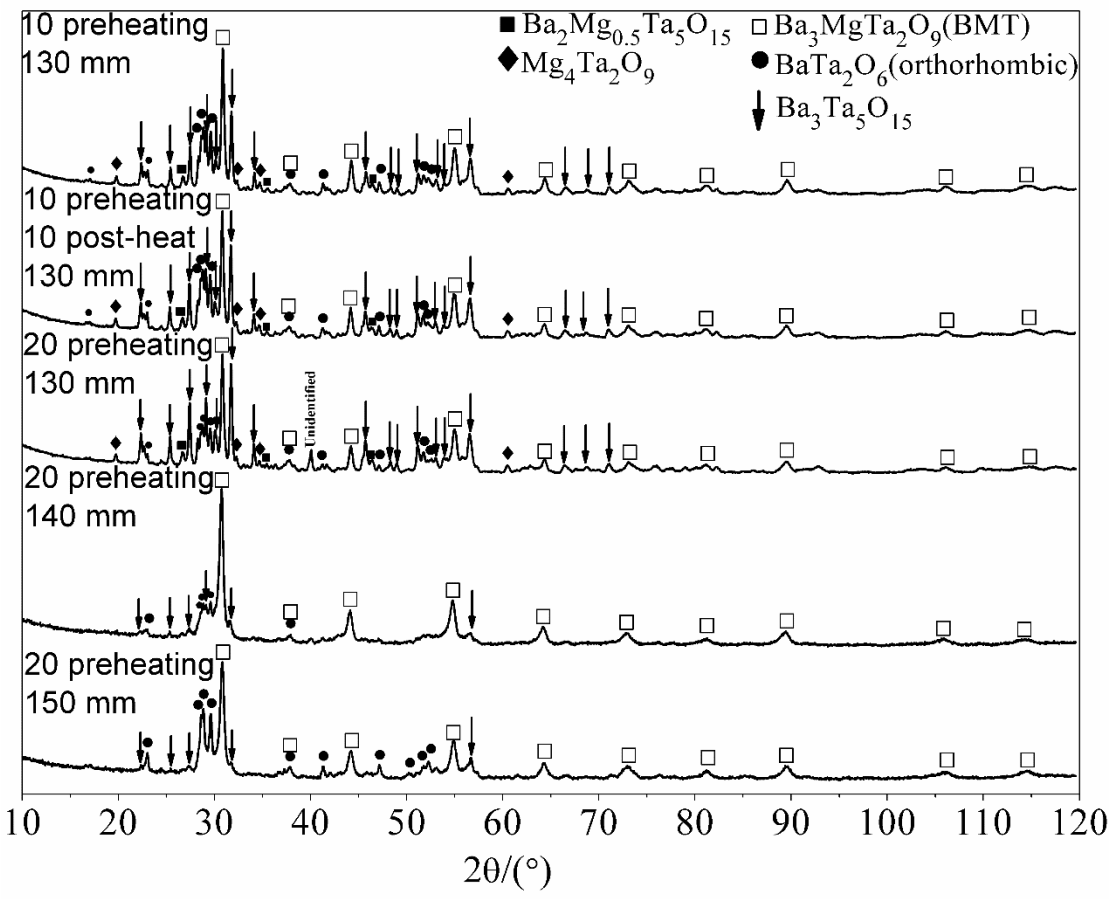

Fig. 10 X-ray diffractograms of as-sprayed coatings prepared by precursor S5 with different pre-heating, post-heating and spraying distances using the same plasma power of 53 kW.

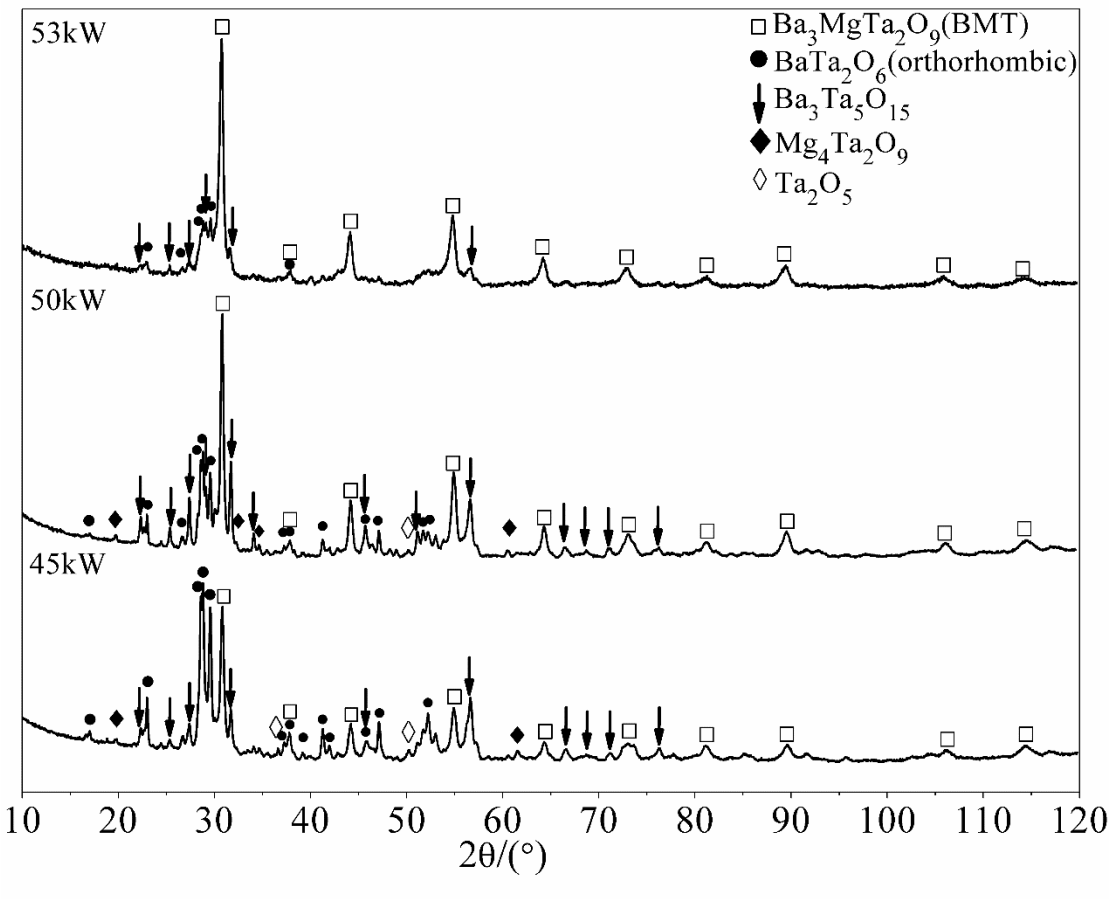

Fig. 11 X-ray diffractograms of as-sprayed coatings prepared by acetate-based precursor (S5) with different plasma powers.

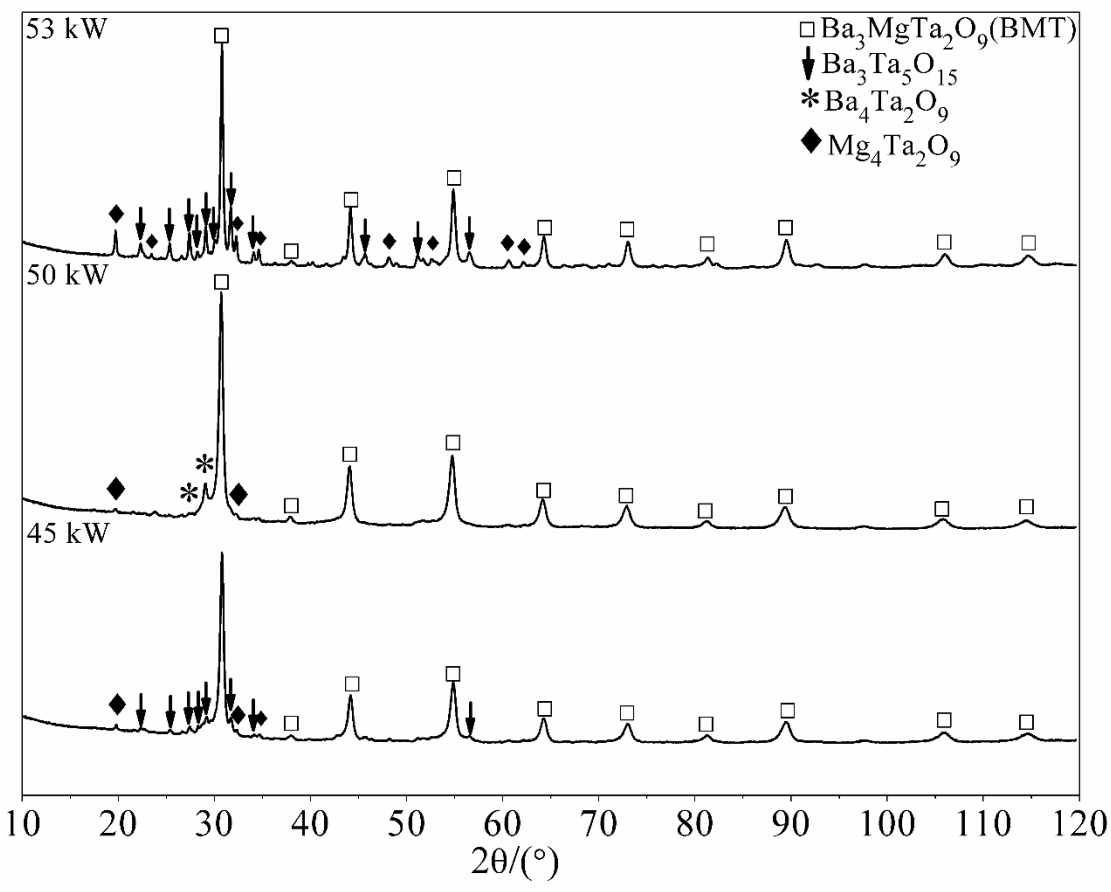

Fig. 12 X-ray diffractograms of as-sprayed coatings prepared by nitrate-based precursor (S4) with different plasma powers.

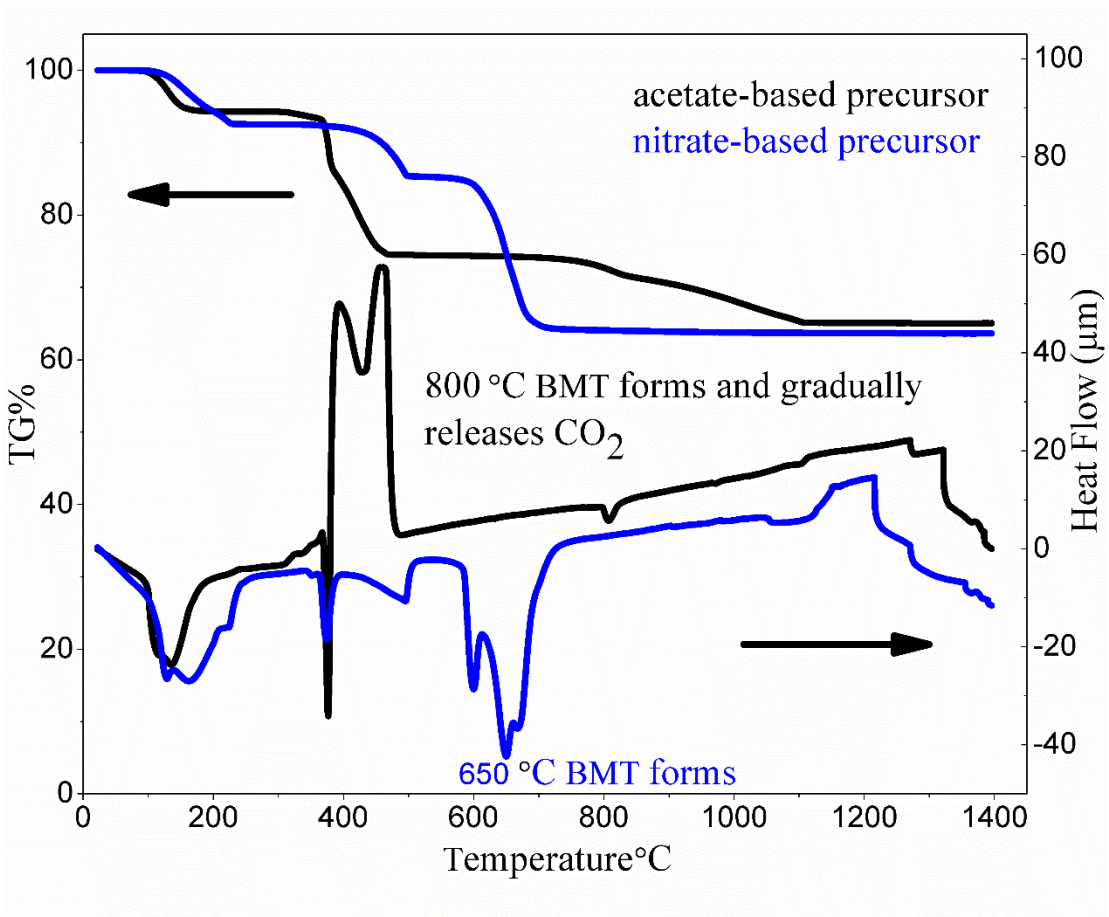

Fig. 13 TG-DTA curves for stoichiometric acetate-based precursor (black) and nitrate-based precursor (blue).

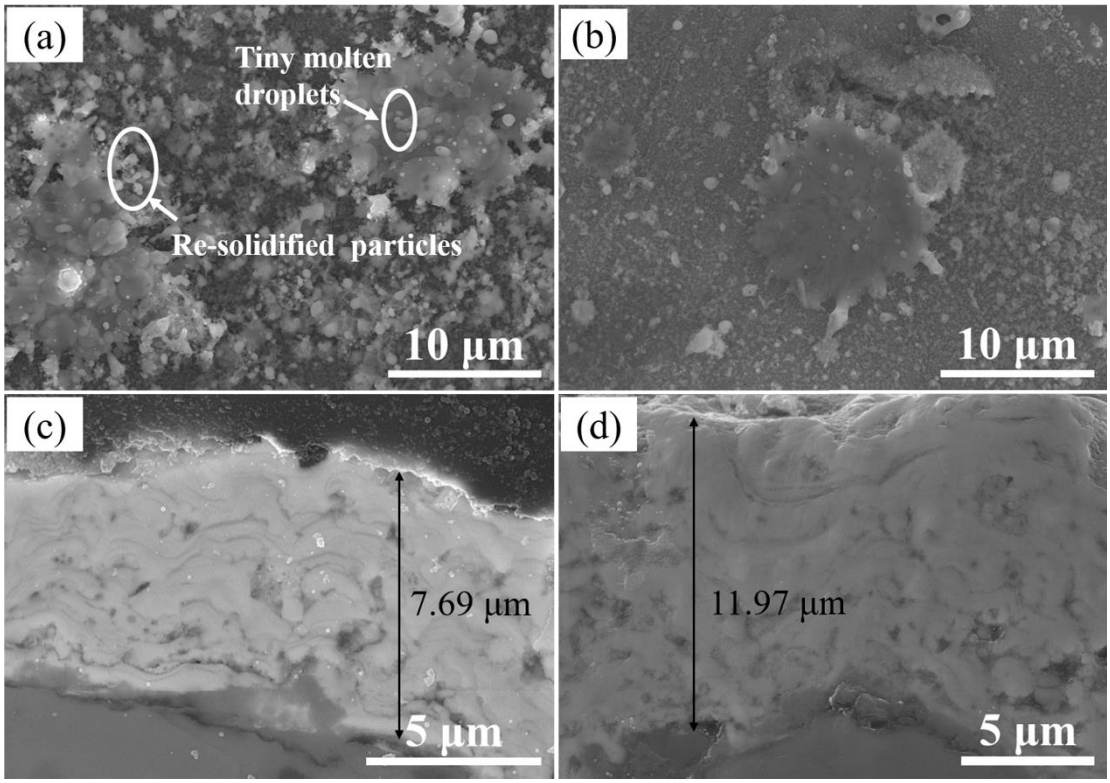

Fig. 14 Splats morphologies and coating cross-sectional images from acetate-based precursors (a) and (c); from nitrate-based precursors (b) and (d).

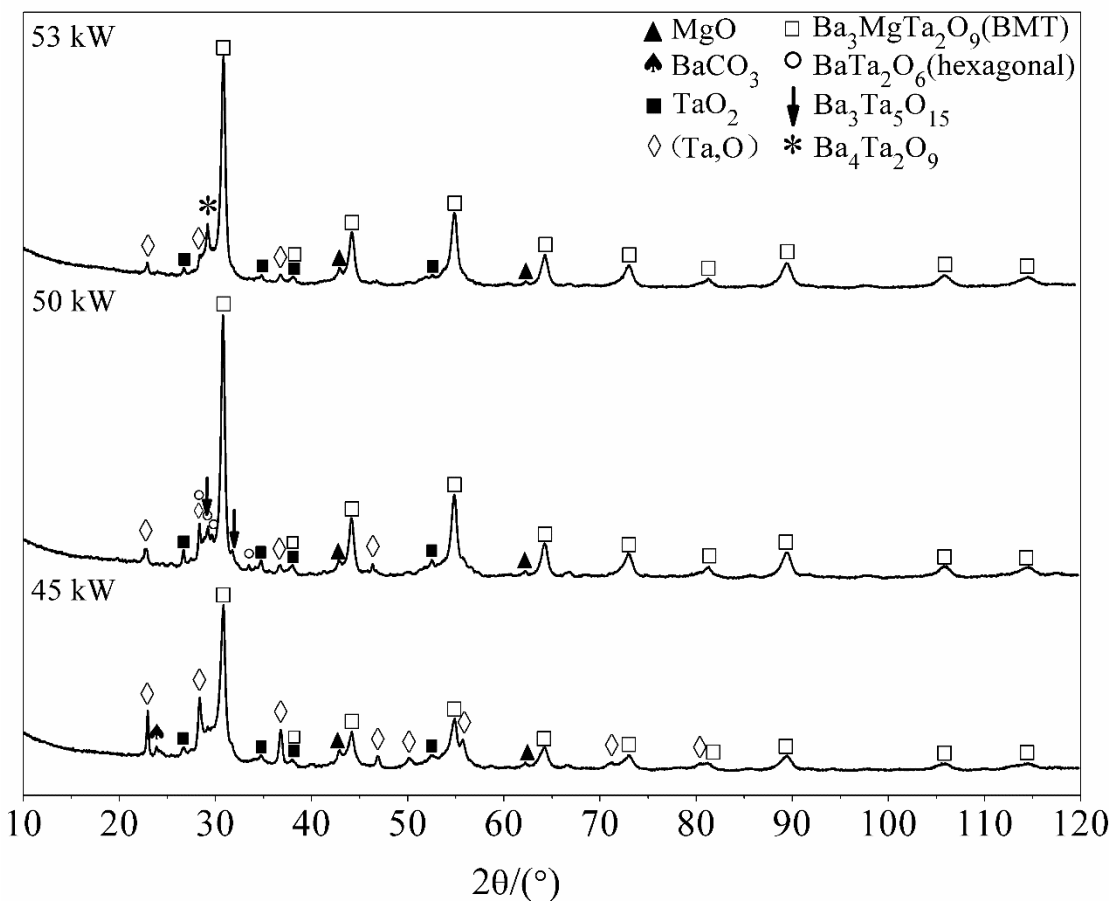

Fig. 15 X-ray diffractograms of as-sprayed coatings prepared by precursor S6 (using spheroidized Ta_2O_5 as Ta precursor) with different plasma powers.

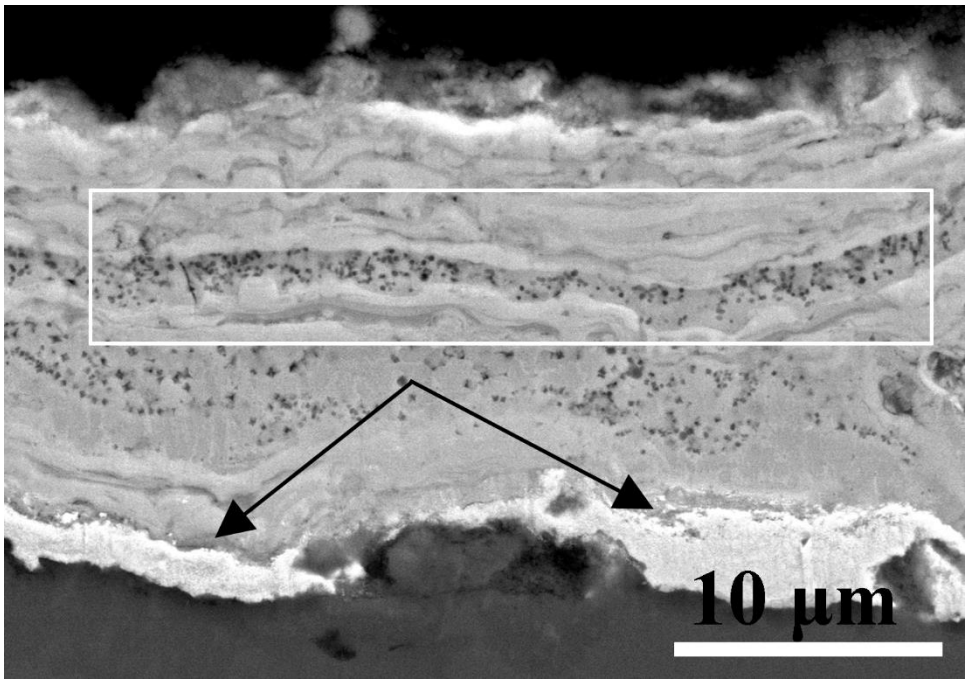

Fig. 16 Cross-sectional images of as-sprayed coating prepared by precursor S6 (using spheroidized Ta_2O_5 as Ta precursor) with a plasma power of 50 kW.

Tables

Table 1 List of suspension /solution precursors combinations and its corresponding plasma power used during spraying.

No.	Solute	Solvent (water: ethanol)	Plasma power
S1	Synthesized BMT powder	1:1	45kw
S2	Nanocrystallized Ta_2O_5, Ba nitrate, Mg nitrate (stoichiometric)	1:1	53kW
S3	Nanocrystallized Ta_2O_5, Ba nitrate, Mg nitrate (1.5 × stoichiometric qty)	1:1	53kW
S4	Nanocrystallized Ta_2O_5, Ba nitrate, Mg nitrate (2 × stoichiometric qty)	1:1	45/50/53kW
S5	Nanocrystallized Ta_2O_5, Ba acetate, Mg acetate (2 × stoichiometric qty)	1:3.6	45/50/53kW
S6	Spheroidized Ta_2O_5, Ba nitrate, Mg nitrate (2 × stoichiometric qty)	1:1	45/50/53kW

Table 2 Plasma parameters for Ta_2O_5 spheroidization and nanocrystallization

	Spheroidization	Nanocrystallization
Sheath gas (Ar)	6 slpm	3 slpm
Sheath gas (O_2)	63 slpm	63 slpm
Sheath gas (He)	No	110 slpm
Central gas (Ar)	23 slpm	23 slpm
Feeding rate	0.2 ± 0.1 g/min	0.5 ± 0.1 g/min
Reactor pressure	33 kPa	80 kPa
Power	43 kW	58 kW

Table 3 Plasma parameters for BMT coating preparation.

Sheath gas (Ar)	6 slpm
Sheath gas (O_2)	63 slpm
Central gas (Ar)	23 slpm
Feeding rate	4 ml/min
Reactor pressure	15 kPa
Power	45/50/53 kW
Stand-off distance	130/140/150 mm
Translational	50 mm/s

Table 4 XPS spectral fitting parameters for different elements and their corresponding position, FWHM, concentration (At. %) and concentration ratio of main elements

	XPS spectral fitting parameters			
Type	Element	Position(eV)	FWHM(eV)	At. %
Synthesized BMT powder	Ba 3d5/2	778.8	3.37	13.65
	Mg 1s	1303.8	2.87	2.67
	Ta 4d	229.8	5.05	8.62
	O 1s	529.8	3.56	54.07
	C 1s	284.8	3.52	20.99
Coating prepared by S1	Ba 3d5/2	778.8	2.94	8.68
	Mg 1s	1303.8	3.24	0.77
	Ta 4d	229.8	4.81	7.32
	O 1s	529.8	3.27	44.16
	C 1s	284.8	2.92	36.92
	Cu 2p3/2	934.8	4.32	2.16
Coating prepared by S2	Ba 3d5/2	779.8	3.11	8.59
	Mg 1s	1304.8	2.98	1.07
	Ta 4d	229.8	4.78	8.75
	O 1s	529.8	3.28	47.44
	C 1s	284.8	3.39	32.75
	Cu 2p3/2	933.8	3.91	1.40

	Ratio of main elements		
Elements	Powder	S1	S2
Mg/Ba	0.2	0.1	0.1
Mg/Ta	0.3	0.1	0.1
Ta/Ba	0.6	0.8	1.1